# Scattering of electromagnetic radiation by three-dimensional periodic arrays of identical particles

**Yu-Lin Xu**

*Jacobs, Orbital Debris Research and Science Operations, Mail Code: JE104, 2224 Bay Area Boulevard, Houston, Texas 77058, USA (yu-lin.xu-1@nasa.gov)*

The generalized multiparticle Mie-solution (GMM), a Lorenz–Mie-type rigorous theory for the scattering of a monochromatic plane wave by an arbitrary configuration of nonintersecting scattering bodies, has lately been revisited and further developed. A recent progress is the initiation of a special version applied to one- and two-dimensional (1D and 2D) periodic arrays (PAs) of identical particles [J. Opt. Soc. Am. A **30**, 1053 (2013)]. As a continuous advance, the present work extends the initiative PA-type solution from 1D and 2D to the more involved three-dimensional (3D) regular arrays. Analytical formulations applicable to the 3D PAs are derived, including the special PA-type explicit expressions for cross sections of extinction, scattering, backscattering, and radiation pressure. The specific PA-version is a complement to the general formulation and solution process of the standard GMM. In either 1D and 2D or 3D cases, the newly devised PA-approach is capable of providing expeditiously theoretical predictions of radiative scattering characteristics for periodic structures consisting of a huge number of identical unit cells, which the general approach of the GMM is unable to handle in practical calculations, owing to excessive computing time and/or computer memory requirements. To illustrate practical applications, sample numerical solutions obtained via the PA-approach are shown for 3D PAs of finite lengths that have $\sim 5 \times 10^7$ component particles, including structures having a rectangular opening. Also discussed is potential future work on the theory and its tests.    © 2014 Optical Society of America

*OCIS codes:*    (290.4210) Multiple scattering; (290.5825) Scattering theory; (260.1180) Crystal optics; (260.1960) Diffraction theory; (260.5430) Polarization.

http://dx.doi.org/10.1364/JOSAA.31.000322

## 1. INTRODUCTION

Analogous to the Mie theory for single homogeneous spheres [1,2], there are widely tested, comprehensive analytical solutions to the ensemble scattering of light and other electromagnetic radiation. The generalized multiparticle Mie-solution (GMM) [3–12], developed more than a decade ago, is such an example for an arbitrary collection of scattering bodies illuminated by a monochromatic plane wave. Constituent units in an ensemble can have arbitrarily mixed intrinsic properties and structures, both physical and geometrical. The only prerequisite is that the $T$-matrices [13–20] of all individual scattering units in their independent scattering (i.e., when they are isolated) are known analytically (such as for spheres) or can be computed with satisfactory precision for given physical and geometrical parameters. As practical implementation of the multibody scattering formulation for the general application to an arbitrary ensemble of scattering entities, a set of FORTRAN computer codes of GMM have been publicly accessible since 2001 [21], and are used and scrutinized by many researchers across a great variety of scientific and technical fields.

Literally, the general scattering formulation of GMM does not place any restriction on the size, shape, material composition, structure, and morphology of the constituent units in an ensemble. Accordingly, all current public-domain computer codes of GMM solve individual (or partial) scattered fields for every component particle in respective particle-centered reference systems. While the generality is advantageous on one hand, there are disadvantages in practical calculations on the other hand, as regards computing time requirements in particular. For an array consisting of $N$ component particles, the required computing time is roughly proportional to $N^2$. An array of $\sim 10^4$ wavelength-sized constituent particles usually needs several days to complete scattering calculations for a single, fixed spatial orientation, using a Dell Precision T7500 desktop computer. When the number of the component particles increases to $\sim 10^5$, $\sim 10$ times larger, it may demand up to a year of computing time. It is inevitable that the multiparticle scattering calculations via the general approach (GA) of GMM encounter a severe limitation on the maximum number of component particles allowed in an ensemble with regard to an acceptable length of computing time period. Moreover, it is also evident that larger numerical errors will be introduced into numerical solutions to an ensemble consisting of a larger number of component particles and with larger overall dimensions. One of the possible causes for this is that multibody scattering calculations involve the evaluation of a huge amount of vector translation coefficients and there could be enormous differences in the magnitudes of this type of coefficients for small and large translation distances.

A special version of the GMM scattering formulation for one- and two-dimensional (1D and 2D) periodic arrays (PAs) of identical particles has been presented in a recent

article [22], which will be referred to as Paper I hereafter. The development of the special PA approach relies on the favorable periodicity of the spatial structures of PAs combined with beneficial features of GMM, such as the direct use of precise phase terms for both incident and scattered radiation when solving far-field scattering. It brings remarkable savings in computing time, in comparison with the GA procedure. Scattering calculations for a PA consisting of $\sim 10^5$ wavelength-sized particles requires only a few minutes to complete. As stressed in Paper I, however, the special PA formulation holds precise merely for PAs of infinite extents that have no edge (and thus lack of practical meanings). For PAs of finite lengths, the trade-off is that the "edge effect" introduces certain numerical errors into numerical solutions, the significance of which depends on the total number of replica units in a PA. As the illustrative examples in Paper I indicate, the edge effect recedes as the number of component particles in a PA increases. In other words, the PA approach provides sufficiently accurate numerical solutions to the finite PAs that have a sufficiently large number of component units (and thus have sufficiently large overall dimensions in comparison with the incident wavelength and the dimensions of an individual unit cell).

The intent of the present work is to extend the PA version of GMM initiated in Paper I to the general three-dimensional (3D) case. As a feasibility study for the intended extension and as suggested in Paper I, the edge effect has been further investigated for 1D and 2D PAs at arbitrary spatial orientations. Numerical solutions obtained from the PA approach are systematically tested against those from the benchmark GA procedure. Outcomes of this study suggest that the diminishing of the edge effect with the increase of the total number of component particles in a PA is independent of the PA's spatial orientation and the intrinsic properties of the component particles. When the total number of particles in a PA reaches certain level, the edge effect begins to fade away and becomes negligible. It is also evident that, to depress the edge effect down to a similar low level, the total number of component particles in a 2D PA must be much larger than that for a 1D PA. Generally speaking, the number of component particles in a PA must be sufficiently large along each dimension in order to obtain satisfactorily accurate numerical solutions via the PA approach. Illustrative numerical examples are given in the next section to show supportive evidence.

Section 3 presents specific scattering solutions to 3D regular particle arrays, giving only final results without detailed derivations. These include the PA-type formulas for cross sections of extinction, scattering, backscattering, and radiation pressure, which are simply the special form of the general and more complicated GMM formulation. To demonstrate the practical implementation of the newly derived analytical formulation, Section 4 provides sample numerical solutions to a 3D PA of $\sim 5 \times 10^7$ identical constituents for three different cases, showing how its scattering behavior responds to the change in the material composition of component particles and its spatial orientation, as well as the polarization state of incident radiation.

A new theoretical development always needs an adequate way to verify and to validate as well as to identify its regime of validity. For 1D and 2D PAs, systematic PA-to-GA comparisons proved to be an effective means to serve such a purpose.

But this type of testing is too time-consuming to be feasible for the 3D case and is not pursued at this stage. To depress the edge effect to a sufficiently low level, i.e., to bring PA and GA numerical solutions sufficiently close to each other, a finite PA must have a much larger number of constituent units when extending to more dimensions. It is highly desirable to be able to calculate 3D PAs that have $>10^6$ wavelength-sized component particles via the standard GA procedure of GMM. Such GA-type scattering calculations would demand an intolerably lengthy computing time (even when computer memory allows) and become impractical for ordinary desktops and laptops at this point. Nevertheless, there are other ways to examine the validity of the formulation, such as to compare with other widely tested and well-established theories in common applications or to compare with corresponding experimental measurements in areas of common interest. Some preliminary consideration and work toward such further study is discussed in Sections 5 and 6.

It is easy to see that the PA-approach of GMM leads to formulations consistent with what is derived from Fourier analysis, as far as the angular distributions of scattered amplitude and intensity are concerned. In this regard and as a starting point for the comparison with existing diffraction theories, Section 5 provides additional numerical examples for 2D and 3D regular arrays with rectangular openings. As it is supposed to be, the predicted scattering patterns in the far field of such spatial structures exhibits familiar features of the Fraunhofer diffraction pattern known for a rectangular aperture. This is by no means a coincidence. Scattering solutions extended from Mie theory struggle to formulate rigorously the interaction of light and other electromagnetic radiation with obstacles of complex forms, on the basis of Maxwell's equations together with appropriate boundary conditions. A scattering theory aims to make testable predictions to scattered field distributions within its range of validity, including the prediction of diffraction patterns universally observed. Since diffraction theories provide analytical interpretations to the same physical phenomena based on seemingly rather different theoretical foundations, it is worthwhile to comprehensively compare with insight between the scattering and diffraction formulations. Besides being a mutual test, such further work might be able to build a bridge to connect the two and help to clarify inherent ambiguity or misconception in the theoretical expositions, if there is any. In addition to concluding remarks, the last Section 6 contains some discussion on the potential further work on the theory and its tests.

## 2. REGIME OF VALIDITY OF THE PA APPROACH: DIMINISHING OF THE EDGE EFFECT FOR 1D AND 2D PERIODIC STRUCTURES

As is shown and clearly stated in related earlier publications [4–12], a distinct feature of the GMM is that its theoretical treatment of far-field scattering uses explicitly and precisely both incident and scattered phase shifts, referring to respective centers of individual component units in an ensemble of scattering bodies. This advantageous feature, together with the spatial periodicity of PAs, helps to radically simplify the scattering solution to periodic structures and leads to the development of the special PA version of GMM [22]. It is worthwhile to emphasize and remind repeatedly that the

PA approach has its range of validity in connection with the edge effect.

Prior to the extension of the PA formulation initiated in Paper I to the general 3D case, the edge effect has been further investigated for finite 1D and 2D PAs at arbitrary, fixed spatial orientations. Reliability of the numerical solutions obtained from the PA approach is examined against the benchmark given by the GA procedure of the standard GMM for different material compositions of the component particles, such as dielectric, nonabsorbing, and perfectly conducting, and for different polarization states of the incident plane wave, as well as for different spatial orientations of a PA in the incident beam. Because the GA-type calculations are awfully time-consuming for an array with a large number of constituent particles, especially when the size parameter of an individual particle is not small, PAs calculated in this investigation are limited to those consisting of $<10^5$ small (wavelength compatible) particles. Results from this study indicate that the total number of component units in a PA is the determinative factor to the edge effect. Although dependent on the size parameter and material composition of the individual constituent particles, as well as on the geometrical structure of a PA, it seems that the edge effect for a 1D array having a few thousand or more replica units is generally negligible. For a 2D array with the total number of replicas between $\sim 10^4$ and $10^5$, the PA-to-GA deviations are roughly at the level of a couple of percent.

## A. Specification of the Spatial Orientation of an Array of Particles

The spatial orientation of a PA, i.e., the position vector of the center of every component particle in the array, is specified by three successive rotations of the reference frame about origin in terms of the Euler-angle triad $(\alpha\beta\gamma)$ from an initial orientation, conveniently chosen prior to the rotation. The convention used here for the rotation matrix in terms of the triad of Euler angles follows what is described in Edmonds [23], which is

$$\mathbf{R}(\alpha\beta\gamma) = \mathbf{R}_z(\gamma)\mathbf{R}_y(\beta)\mathbf{R}_z(\alpha). \tag{1}$$

The rotation about the $z$ or $y$ axis is defined by

$$\mathbf{R}_z(\alpha) = \begin{bmatrix} \cos\alpha & \sin\alpha & 0 \\ -\sin\alpha & \cos\alpha & 0 \\ 0 & 0 & 1 \end{bmatrix}, \quad \mathbf{R}_y(\beta) = \begin{bmatrix} \cos\beta & 0 & -\sin\beta \\ 0 & 1 & 0 \\ \sin\beta & 0 & \cos\beta \end{bmatrix}. \tag{2}$$

Accordingly, the position vector of every component particle center $l$ in an array under calculation is given by $\mathbf{d}^l = \hat{\mathbf{e}}_x X^l + \hat{\mathbf{e}}_y Y^l + \hat{\mathbf{e}}_z Z^l$, where $\hat{\mathbf{e}}$ designates a unit vector and

$$\begin{pmatrix} X^l \\ Y^l \\ Z^l \end{pmatrix} = \mathbf{R}(\alpha\beta\gamma) \begin{pmatrix} X_0^l \\ Y_0^l \\ Z_0^l \end{pmatrix}, \tag{3}$$

with $(X_0^l, Y_0^l, Z_0^l)$ being the coordinates at the initial orientation.

## B. Diminishing of the Edge Effect for 1D and 2D PAs at an Arbitrary Spatial Orientation: Two Examples

Two examples are presented below to show that the edge effect declines and dies away as the total number of

component particles in a PA increases. The first is a 1D linear array and the second is a 2D square array of identical spheres. These two finite PAs are calculated using both GA and PA approaches when the total number of component spheres gradually increases up to $\sim 30,000$, which keeps the maximum computing time for a single PA at a single fixed orientation no more than about a month for the GA-type calculations. Numerical solutions provided by the special PA approach become practically identical to those calculated through the GA procedure when the total number of component particles in the 1D array is $\gtrsim 3000$. The PA-to-GA deviations for the 2D array with a similar number of constituent particles are larger than the 1D array, which is simply due to the increase in the number of dimensions.

Shown in Fig. 1 is the regular 1D array of identical dielectric spheres, which are nonabsorbing, having a refractive index of 1.6, and of 1 mm diameter. The spheres are equally 1 mm apart, i.e., neighboring spheres are in contact. The $z$-propagating incident plane wave is of 31.416 mm wavelength and each individual sphere has a size parameter of 0.1. The Euler-angle triad specifying the orientation of the linear array is $(0°,45°,20°)$. In its initial orientation, all sphere centers are aligned along the $x$ axis. The left panel shows the PA-to-GA deviations of the calculated cross sections of extinction, backscattering, and radiation pressure versus the total number of component spheres in the linear chain, when the incident wave is unpolarized. The right panel shows the CPU time required by both the GA- and PA-type calculations.

Similarly, Fig. 2 is for the square array of identical spheres that are of 1 mm diameter and complex refractive index (1.6, 0.1). The Euler-angle triad defining the orientation of this 2D array is $(0°,20°,30°)$. Its initial orientation is such that all the component sphere centers are in the initial $x$–$y$ plane with rows parallel to the $x$ axis and columns parallel to the $y$ axis and equally spaced by 1 mm in each row and column. Compared with the results shown in Fig. 1, it is evident that a 2D array needs a much larger number of component particles than a 1D array in order to obtain a comparable accuracy for the numerical solutions.
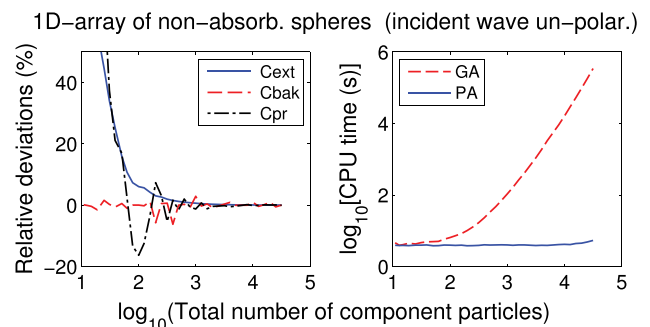


Fig. 1. Comparison between PA- and GA-type GMM scattering calculations for a linear chain of identical nonabsorbing spheres, illuminated by a monochromatic plane wave of wavelength 31.416 mm. Its spatial orientation is specified by the Euler-angle triad $(0°,45°,20°)$, referring to the initial orientation of $x$ alignment, i.e., all sphere centers are initially aligned along the $x$ axis. The component spheres are of 1 mm diameter and of refractive index 1.6, equally spaced 1 mm apart. The left panel shows the relative PA-to-GA deviations (%) of the calculated cross sections of extinction, backscattering, and radiation pressure when the total number of component spheres in the 1D array gradually increases. The right panel shows the CPU time elapsed in both the GA- and PA-type calculations.
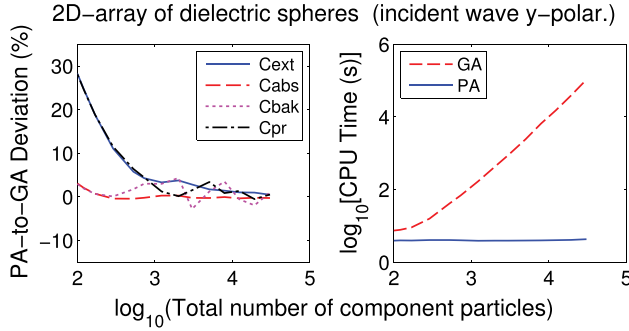
Fig. 2.   Similar to Fig. 1 but for square arrays of densely packed identical spheres of 1 mm diameter and of complex refractive index (1.6, 0.1). The orientation of the 2D arrays is specified by the Euler-angle triad (0°,20°,30°). Their initial orientation is such that all component sphere centers are in the initial $x$–$y$ plane with rows parallel to the $x$ axis and columns parallel to the $y$ axis.

# 3. SCATTERING FORMULATIONS FOR 3D PERIODIC STRUCTURES

Consider a 3D array of identical particles illuminated by a plane wave of wavelength $\lambda$:

$$\mathbf{E}^{\mathrm{inc}} = \mathbf{E}_0 \, \exp(i\hat{\mathbf{k}} \cdot \mathbf{r} - i\omega t), \qquad (4)$$

where $i = \sqrt{-1}$, $\mathbf{r}$ is the position vector, and $\hat{\mathbf{k}}$ is the unit incident vector. As usual, the harmonic time term $\exp(-i\omega t)$ will be suppressed hereafter. In a primary reference system (PRS), the incident plane wave propagates in the direction specified by the spherical coordinates $(\vartheta^{\mathrm{inc}}, \varphi^{\mathrm{inc}})$ and the unit incident vector can be written as

$$\hat{\mathbf{k}} = \hat{\mathbf{e}}_x \sin \vartheta^{\mathrm{inc}} \cos \varphi^{\mathrm{inc}} + \hat{\mathbf{e}}_y \sin \vartheta^{\mathrm{inc}} \sin \varphi^{\mathrm{inc}} + \hat{\mathbf{e}}_z \cos \vartheta^{\mathrm{inc}}. \qquad (5)$$

When $\vartheta^{\mathrm{inc}} = 0$, $\hat{\mathbf{k}} = \hat{\mathbf{e}}_z$, the incident wave vector points to the positive $z$ direction, which will be referred to as the incident reference system (IRS). As defined earlier, the spatial orientation of the array in a PRS is specified by the rotation of the reference frame in terms of the triad of Euler angles $(\alpha\beta\gamma)$. Given the initial coordinates $(X_0^l, Y_0^l, Z_0^l)$ of every component particle center $l$, their position vectors in the PRS, i.e., the coordinates $(X^l, Y^l, Z^l)$ in the PRS, are determined by Eq. (3). Recall that, in the PA-type of formulation, the total scattered far-field coefficients, $a_{mnp}$, and the total scattering amplitude matrix $\mathbf{S}$ of a PA consisting of $L$ identical particles are approximately [22]

$$a_{mnp} = a_{mnp}^l \cdot \Phi(\theta, \phi), \qquad \mathbf{S} = \mathbf{S}^l \cdot \Phi(\theta, \phi),$$

$$\Phi(\theta, \phi) = \sum_{j=1}^{L} \exp[i\mathbf{d}^j \cdot (\hat{\mathbf{k}} - \hat{\mathbf{r}})]. \qquad (6)$$

Here, $a_{mnp}^l$ and $\mathbf{S}^l$ represent, respectively, the partial scattering coefficients and the individual scattering amplitude matrix of any component particle $l$, $\mathbf{d}^j$ is the position vector of component particle center $j$, $\theta$ and $\phi$ are the two angular polar coordinates, and $\hat{\mathbf{r}}$ is the unit position vector. One needs always to bear in mind that, throughout this paper, all involved

linear dimensions are normalized (i.e., multiplied) by the wave number $k = 2\pi/\lambda$.

The total incident and scattered phase term $\Phi$ in Eq. (6) involves only the incident direction and the geometrical structure of an array and is independent of the scattering behavior of component particles. It varies with direction and is generally a function of the polar coordinates $\theta$ and $\phi$. This section provides explicit formulas for the total phase term $\Phi$ of 3D PAs. Also presented are analytical expressions for cross sections of extinction, scattering, backscattering, and radiation pressure, derived specifically to be applicable to the periodic structures. All of these are given in the final form with no lengthy derivations.

## A. Total Incident and Scattered Phase Shift Term of a 3D PA

The 3D PA under consideration is a cubic array consisting of $L = Nx \cdot Ny \cdot Nz$ identical particles. Its initial orientation is such that the three pairs of "surfaces" are parallel to the $x$–$y$, $y$–$z$, and $x$–$z$ planes, respectively. In the initial frame of reference, component particles are equally spaced by $\Delta x$, $\Delta y$, and $\Delta z$, respectively, in the three primary directions parallel to the $x$, $y$, and $z$ axes. The maximum physical dimensions of the array are thus, respectively, $N_x \Delta x$, $N_y \Delta y$, and $N_z \Delta z$ in the $x$, $y$, and $z$ directions. For such a regular 3D array with its orientation in a PRS defined by the Euler-angle triad $(\alpha\beta\gamma)$, the function $\Phi$ takes the form

$$\Phi(\theta, \phi) = \Phi x \cdot \Phi y \cdot \Phi z, \qquad \Phi x = \frac{\sin(Nx\Delta x/2 \cdot u_x)}{\sin(\Delta x/2 \cdot u_x)},$$

$$\Phi y = \frac{\sin(Ny\Delta y/2 \cdot u_y)}{\sin(\Delta y/2 \cdot u_y)}, \qquad \Phi z = \frac{\sin(Nz\Delta z/2 \cdot u_z)}{\sin(\Delta z/2 \cdot u_z)}, \quad (7)$$

where

$$u_x = t_1 \cos \alpha - s_1 \sin \alpha, \qquad u_y = t_1 \sin \alpha + s_1 \cos \alpha,$$

$$u_z = \cos \eta(\beta, \pi - \gamma; \vartheta^{\mathrm{inc}}, \varphi^{\mathrm{inc}}) - \cos \eta(\beta, \pi - \gamma; \theta, \phi), \qquad (8)$$

and

$$t_1 = \cos \eta\left(\beta - \frac{\pi}{2}, \pi - \gamma; \vartheta^{\mathrm{inc}}, \varphi^{\mathrm{inc}}\right)$$
$$- \cos \eta\left(\beta - \frac{\pi}{2}, \pi - \gamma; \theta, \phi\right),$$
$$s_1 = \sin \vartheta^{\mathrm{inc}} \cdot \sin(\gamma + \varphi^{\mathrm{inc}}) - \sin \theta \cdot \sin(\gamma + \phi), \qquad (9)$$

with $\cos \eta(\beta, \alpha; \vartheta, \varphi) = \sin \beta \sin \vartheta \cos(\alpha - \varphi) + \cos \beta \cos \vartheta$.

For the special case of normal incidence in the IRS, $(\alpha\beta\gamma) = (000)$, $\vartheta^{\mathrm{inc}} = \varphi^{\mathrm{inc}} = 0°$, and we have

$$\Phi(\theta, \phi) = \frac{\sin(Nx\Delta x/2 \cdot \sin \theta \cos \phi)}{\sin(\Delta x/2 \cdot \sin \theta \cos \phi)}$$
$$\times \frac{\sin(Ny\Delta y/2 \cdot \sin \theta \sin \phi)}{\sin(\Delta y/2 \cdot \sin \theta \sin \phi)} \frac{\sin[Nz\Delta z/2 \cdot (1 - \cos \theta)]}{\sin[\Delta z/2 \cdot (1 - \cos \theta)]}. \qquad (10)$$

For 2D PAs, $Nz = 1$, $\Delta z = 0$, and $\Phi z \equiv 1$. Similarly, for 1D PAs, $Ny = Nz = 1$, $\Delta y = \Delta z = 0$, so that $\Phi_y = \Phi_z \equiv 1$.

For 1D and 2D PAs, Eqs. ([7](#))–([10](#)) reduce to what given in Paper I.

## B. Scattering in Exact Forward and Backward Directions: Total Extinction and Backscattering Cross Sections

Radiative scattering in the exact forward and backward directions has distinct features that other directions do not possess. Without loss of generality, it is advantageous to formulate the scattering in these two special cases of $\theta = 0°$ and $180°$ in IRS, which are both independent of $\phi$. For the forward scattering in the direction of $\theta = 0°$ in the IRS, $\hat{\mathbf{r}} = \hat{\mathbf{k}}$. It follows from Eqs. ([7](#))–([9](#)) that $u_x = u_y = u_z \equiv 0$, and $\Phi(0°) \equiv L = Nx \cdot Ny \cdot Nz$. These result in the following simple formulas for the scattered amplitude in this particular direction, $S(0°) = S_1(0°) = S_2(0°)$, and for the total extinction cross-section $C_{\text{ext}}$ of a PA:

$$S(0°) = L \cdot S^l(0°), \quad C_{\text{ext}} = L \cdot C_{\text{ext}}^l, \quad C_{\text{ext}}^l = \frac{4\pi}{k^2} \operatorname{Re} S^l(0°), \tag{11}$$

where, $S^l(0°)$, the forward scattered amplitude of an individual component particle, is given by [[3](#)–[12](#)]

$$S^l(0°) = \sum_{n=1}^{N_{\max}} \sum_{p=1}^{2} \frac{\sqrt{2n+1}}{2} \times [a_{1np}^{l(\beta_p)} \exp(i\beta_p) + (-1)^p a_{-1np}^{l(\beta_p)} \exp(-i\beta_p)], \tag{12}$$

with $\beta_p$ being the linear polarization angle of the incident plane wave that is either $0°$ or $90°$. The extinction cross section of a PA consisting of $L$ component particles is exactly $L$ times larger than that of an individual component particle. However, the forward scattered intensity becomes $L^2$ times stronger than the individual one, which explains the common observation of "forward scattering enhancement."

In the exact backward direction of $\theta = 180°$, $\hat{\mathbf{r}} = -\hat{\mathbf{k}}$, $S(180°) = S_1(180°) = -S_2(180°)$, and Eqs. ([7](#))–([9](#)) tell us that

$$u_x = 2 \sin \beta \cos \alpha, \quad u_y = 2 \sin \beta \sin \alpha, \quad u_z = 2 \cos \beta, \tag{13}$$

and, thus,

$$\Phi(180°) = \frac{\sin(Nx\Delta x \cdot \sin \beta \cos \alpha)}{\sin(\Delta x \cdot \sin \beta \cos \alpha)} \times \frac{\sin(Ny\Delta y \cdot \sin \beta \sin \alpha)}{\sin(\Delta y \cdot \sin \beta \sin \alpha)} \frac{\sin(Nz\Delta z \cdot \cos \beta)}{\sin(\Delta z \cdot \cos \beta)}. \tag{14}$$

As a result, for the backscattering cross section, $C_{\text{bak}}$, which is the important quantity of radar cross section in mono-static radar observations, we obtain

$$C_{\text{bak}} = \frac{4\pi}{k^2} |S(180°)|^2, \quad S(180°) = S^l(180°)\Phi(180°), \tag{15}$$

where [[3](#)–[12](#)]

$$S^l(180°) = \sum_{n=1}^{N_{\max}} \sum_{p=1}^{2} (-1)^{n+p} \frac{\sqrt{2n+1}}{2} \times \left[ a_{1np}^{l(\beta_p)} \exp(i\beta_p) + (-1)^p a_{-1np}^{l(\beta_p)} \exp(-i\beta_p) \right]. \tag{16}$$

Again, the incident linear polarization angle $\beta_p$ in Eq. ([16](#)) is either $0°$ or $90°$. In the special case of normal incidence in IRS, $(\alpha\beta\gamma) = (000)$,

$$\Phi(180°) = Nx \cdot Ny \cdot \frac{\sin(Nz \cdot \Delta z)}{\sin \Delta z}. \tag{17}$$

Unlike in the forward direction, $\Phi(0°) \equiv L$, in the backward direction, the value of $\Phi(180°)$ is dependent on the geometrical structure of a PA, which reaches $L$ only when the last term on the right-hand side of Eq. ([17](#)) approaches to 1. When $\Delta z$ is sufficiently small, $\sin \Delta z \to \Delta z$, $\Phi(180°) \to L \cdot \text{sinc}(Nz\Delta z)$. It is therefore not surprising that there are strong and weak backscatters, depending on the value of $\text{sinc}(Nz\Delta z)$, where $\text{sinc}(x) = \sin x / x$. Similar to the forward scattering at $\theta = 0°$, this explains why there also exists the phenomenon known as "backscattering enhancement."

## C. Total Scattering Cross Section $C_{\text{sca}}$ and the Asymmetry Parameter $\overline{\cos \theta}$

From the general GMM formulation for the total scattering cross section of an arbitrary aggregate of scattering bodies [[3](#)–[12](#)], it is easy to show that the total scattering cross section of a PA takes the special form $C_{\text{sca}} = L \cdot C_{\text{sca}}^l$, where

$$C_{\text{sca}}^l = \frac{4\pi}{k^2} \operatorname{Re} \sum_{n=1}^{N_{\max}^l} \sum_{m=-n}^{n} \sum_{p=1}^{2} a_{mnp}^{l*} \tilde{a}_{mnp}^{(l)}, \tag{18}$$

$$\tilde{a}_{mnp}^{(l)} = \sum_{n'=1}^{N_{\max}^l} \sum_{m'=-n'}^{n'} \sum_{p'=1}^{2} \tilde{C}_{mnpm'n'p'}^l a_{m'n'p'}^l,$$

$$\tilde{C}_{mnpm'n'p'}^l = \sum_{j=1}^{L} \exp(i\hat{\mathbf{k}} \cdot \mathbf{d}^{lj}) \tilde{A}_{mnpm'n'p'}^{lj}, \tag{19}$$

with $\mathbf{d}^{lj} = \mathbf{d}^j - \mathbf{d}^l$. In the above Eq. ([19](#)), $\tilde{A}_{mnpm'n'p'}^{lj}$ is a type of vector translation coefficient, which can be expressed in an integral form [[6](#),[10](#),[12](#)]:

$$\tilde{A}_{mnpm'n'p'}^{lj} = \frac{1}{4\pi} \int_0^{2\pi} \int_0^{\pi} \sin \theta d\theta d\phi \times \exp(i\hat{\mathbf{r}} \cdot \mathbf{d}^{jl}) \exp[i(m'-m)\phi] \times [\tilde{\tau}_{mnp}(\theta)\tilde{\tau}_{m'n'p'}(\theta) + \tilde{\tau}_{mn,3-p}(\theta)\tilde{\tau}_{m'n',3-p'}(\theta)], \tag{20}$$

where $\tilde{\tau}_{mnp}$ represents modified angular functions [[10](#)–[12](#),[22](#)]. Note that there is another type of vector translation coefficient $A_{mnpm'n'p'}^{lj}$ for use in the transformation of the scattered waves from particle $j$ into incident waves for particle $l$. The only difference between $\tilde{A}_{mnpm'n'p'}^{lj}$ and $A_{mnpm'n'p'}^{lj}$ is that the former is associated with the spherical Bessel function of the first kind and the latter with the spherical Hankel function of the first kind. Consequently, the coefficients $\tilde{C}_{mnpm'n'p'}^l$

appearing in Eq. (19) is similar to but slightly different from $C^l_{mnpm'n'p'}$ discussed in Paper I. Future work should be able to find an efficient means to evaluate in an integrated manner both the $\tilde{C}^l_{mnpm'n'p'}$ and $C^l_{mnpm'n'p'}$ coefficients, in order to bypass time-consuming computations involving individually the large amount of component particles.

Calculation of the total cross section for radiation pressure, $C_{pr} = C_{ext} - C_{sca}\overline{\cos\theta}$, requires evaluation of the total asymmetry parameter $\overline{\cos\theta}$. In IRS, $\overline{\cos\theta} = L \cdot \overline{\cos\theta^l}$ for a PA with $L$ component particles and [6,12]

$$\overline{\cos\theta^l} = \frac{4\pi}{k^2 C_{sca}} \operatorname{Re} \sum_{n=1}^{N^l_{max}} \sum_{m=-n}^{n} \sum_{p=1}^{2} a^{l*}_{mnp} \tilde{s}^{(l)}_{mnp}, \qquad (21)$$

where [6,12]

$$\tilde{s}^{(l)}_{mnp} = f_1 \tilde{a}^{(l)}_{mn,3-p} + f_2 \tilde{a}^{(l)}_{m,n+1,p} + f_3 \tilde{a}^{(l)}_{m,n-1,p}, \qquad (22)$$

with the three $f$-coefficients given by

$$f_1 = \frac{m}{n(n+1)},$$
$$f_2 = \frac{1}{n+1}\left[\frac{n(n+2)(n-m+1)(n+m+1)}{(2n+1)(2n+3)}\right]^{1/2},$$
$$f_3 = \frac{1}{n}\left[\frac{(n-1)(n+1)(n-m)(n+m)}{(2n-1)(2n+1)}\right]^{1/2}. \qquad (23)$$

The absorption cross section for an entire array is simply $C_{abs} = C_{ext} - C_{sca}$, and for an individual component, $C^l_{abs} = C^l_{ext} - C^l_{sca}$. There also exist explicit formulas for the absorption cross section of an individual component particle [4,7], offering an alternative way to calculate $C^l_{abs}$ as a check on the accuracy of the numerical solutions.

# 4. ILLUSTRATIVE NUMERICAL EXAMPLES

The new PA-series FORTRAN codes of GMM mentioned in Paper I have been expanded to the 3D case by including the implementation of the scattering formulation for 3D PAs described above. Illustrative numerical results presented in this section are obtained from the newly extended FORTRAN code "gmm01_PA.f." These example numerical solutions are for the same cubic array of $365 \times 365 \times 365$ densely packed, identical spheres of 1 mm diameter, illuminated by a monochromatic plane wave of wavelength 31.416 mm. In every 365-sphere linear chain along each of the three dimensions, sphere centers are equally spaced 1 mm apart, i.e., neighboring spheres are in contact. Recall that the initial orientation of the cubic array is such that its three pairs of "surfaces" are parallel to the $x$–$y$, $y$–$z$, and $x$–$z$ planes, respectively. Recall also that the actual orientation of the PA to be calculated is defined by the Euler-angle triad $(\alpha\beta\gamma)$ with respect to its initial orientation. When $(\alpha\beta\gamma) = (000)$, it is in the initial orientation. As listed in Table 1, three different cases are calculated for the regular 3D array, regarding the material type of the component spheres and its spatial orientation. The IRS is used for all the scattering calculations involved in this work, meaning that the incident vector always points to the positive $z$ direction.

**Table 1. Three Cases Calculated Using the FORTRAN Program "gmm01_PA.f" for a Regular Cubic Array of $365 \times 365 \times 365$ Identical Spheres**

| Case No. | Material of Component Particles | Refractive Index | Spatial Orient. $(\alpha\beta\gamma)$ |
|---|---|---|---|
| 1 | Dielectric, nonabsorbing | (1.6, 0) | (000) |
| 2 | Metallic | (200, 200) | (000) |
| 3 | Metallic | (200, 200) | (0°, 20°, 30°) |

Figures 3–5 refer to Case 1, in which the cubic array is in its initial orientation and the dielectric component spheres are nonabsorbing, having a refractive index of (1.6, 0). Figure 3 presents the Mueller matrix element $S_{11}$ as a function of the angular polar coordinates $\theta$ and $\phi$, or the scattering and azimuth angles in the IRS, shown as the variation with $x = \sin\theta\cos\phi$ and $y = \sin\theta\sin\phi$. There are four panels in Fig. 3. The left two are for the forward hemisphere of $0° \leq \theta \leq 90°$ (with $\theta = 0°$ being the exact forward scattering direction) and the right two are for the backward hemisphere of $90° \leq \theta \leq 180°$ (with $\theta = 180°$ being the exact backward scattering direction). The lower two panels are equivalent to the upper two, presenting the same data but in an alternative way. According to the definition of the Mueller matrix [24–26], $S_{11}$ represents the scattered intensity in the far field when the incident plane wave is unpolarized. We see in Fig. 3 that scattered intensities surge precipitously in the central area in the vicinity of the exact forward and backward directions ($\theta = 0°$ or $180°$). This is due to the forward scattering and backscattering enhancements discussed earlier. The overwhelming central peak covers up the variations of scattering intensity in other directions and makes the patterns looking prosaic and featureless. In fact, this type of scattered intensity pattern, full of precious information on the physical and geometrical properties of the scattering bodies, is never
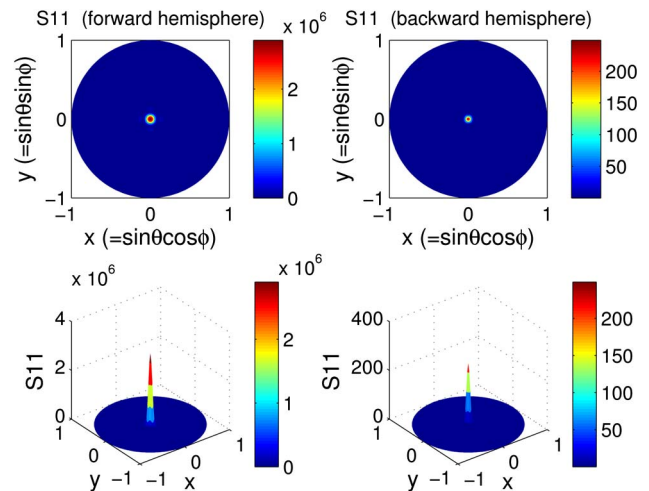


Fig. 3. Dependence of the Mueller matrix element $S_{11}$ on scattering angle $\theta$ and azimuth angle $\phi$ (shown as variation with $x = \sin\theta\cos\phi$ and $y = \sin\theta\sin\phi$) for a cubic array of $365 \times 365 \times 365$ densely packed identical spheres of 1 mm diameter, illuminated by a monochromatic plane wave of wavelength 31.416 mm. The cubic array is in its initial orientation and the dielectric component spheres are nonabsorbing, having a refractive index of 1.6. This is Case 1 as listed in Table 1. The lower two panels are equivalent to the upper two, simply presenting the same data in an alternative way.
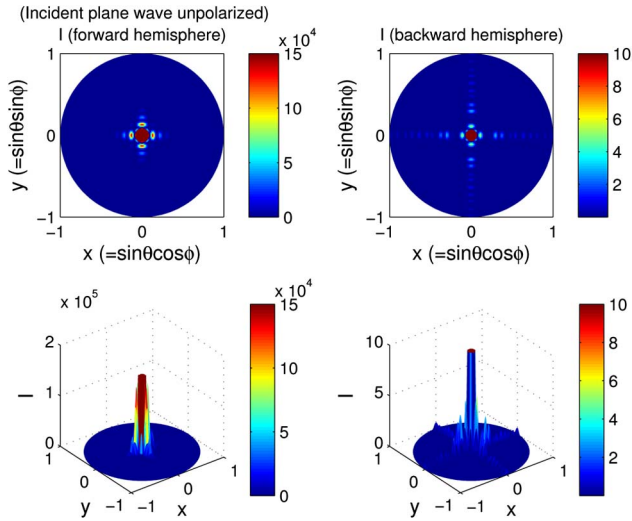
Fig. 4.   Dependence of the Stokes parameter $I$ on scattering angle $\theta$ and azimuth angle $\phi$ (shown as variation with $x = \sin\theta\cos\phi$ and $y = \sin\theta\sin\phi$) for the same cubic array and for the same Case 1 as shown in Fig. 3. The incident plane wave is unpolarized. Note that the tip of the central peak is removed in both the forward and backward directions, as shown in the figures. Otherwise, all the figures would look exactly the same as those in Fig. 3.
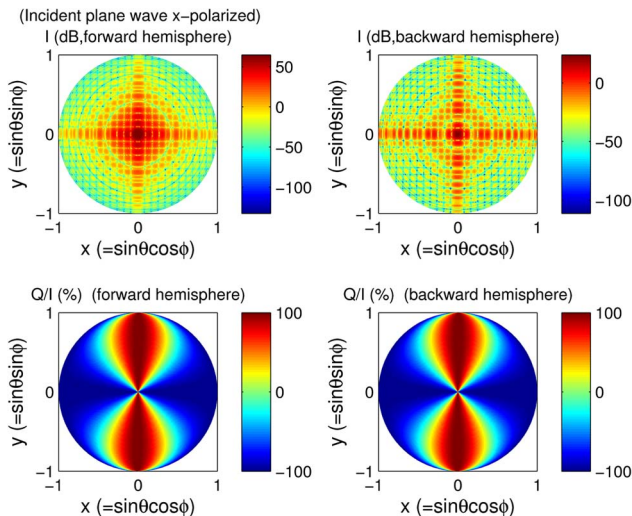


Fig. 5.   Dependence of the Stokes parameters $I$ and $Q$ on scattering angle $\theta$ and azimuth angle $\phi$ (shown as variation with $x = \sin\theta\cos\phi$ and $y = \sin\theta\sin\phi$) for the same cubic array in the same Case 1 as shown in Figs. 3 and 4. The incident plane wave is linearly $x$-polarized. The parameter $I$ is shown in dB.

featureless. There are different ways to disclose graphically the colorful angular distribution pattern of scattered intensity. One way is to snap off a bit the sharp tip of the central peak, which is, in the terminology of photography, to make the small central region overexposed. Figure 4 is such an example, which shows the dependence of the Stokes parameter $I$ on $\theta$ and $\phi$ for the same Case 1 when the incident wave is unpolarized. Compared to Fig. 3, it is easy to notice that the tip of the central peak is removed in both the forward and backward directions in Fig. 4. The maximum value of $I$ shown in Fig. 4 is $1.5 \times 10^5$ in the left two panels and 10 in the two right panels, meaning that all $>1.5 \times 10^5$ values are set to $1.5 \times 10^5$ in

forward directions and all $>10$ values are set to 10 in backward directions. These involve only the tiny area surrounding the exact forward and backward directions. Were the Stokes parameter $I$ shown in Fig. 4 intact, Figs. 3 and 4 would look exactly the same. With the very tip nipped off, patterns unseen in Fig. 3 are uncovered. Another option is to exhibit the intensity pattern in logarithm scale, as in Fig. 5, which displays the Stokes parameters $I$ and $Q$ versus $\theta$ and $\phi$ for the same Case 1 when the incident wave is linearly $x$ polarized. The parameter $I$ appearing in Fig. 5 is in decibels, i.e., $10\log_{10}(I)$ instead of the value of $I$ itself.

Figure 6 is for Case 2, showing the angular distribution of the Stokes parameters $I$ and $Q$ over $\theta$ and $\phi$ (again as the variation with $x = \sin\theta\cos\phi$ and $y = \sin\theta\sin\phi$) when the incident plane wave is linearly $y$ polarized. As listed in Table 1, the only difference between Case 1 and Case 2 is the material type of the component spheres. In Case 2, the spheres are metallic, electrically conducting. The complex refractive index of (200, 200) is used in the related scattering calculations. Note that to present the Stokes parameter $I$ in the same way as in Fig. 4, the maximum value shown in the upper two panels of Fig. 6 are $1.5 \times 10^5$ and 30, respectively, as labeled in the figures. The scattered intensity patterns in Figs. 6 and 4 have both similarities and differences, reflecting the same overall shape and orientation of the scattering entity and the dependence of scattering behaviors on the material type of component particles in a PA.

Sample numerical results for Case 3 are presented in Figs. 7 and 8. Case 3 differs from Case 2 in the PA's spatial orientation only. In Case 3, the Euler-angle triad, defining the orientation of the cubic array of metallic spheres, is $(\alpha\beta\gamma) = (0°, 20°, 30°)$, instead of (000) for Case 2. Shown in Fig. 7 are the Mueller matrix elements $S_{11}$ (in decibels) and $S_{22}$ versus $\theta$ and $\phi$. Figure 8 is similar to Fig. 6 but for Case 3 with the incident wave right-circularly polarized. We see clearly from the figures that scattering characteristics of a finite PA are strongly dependent on its orientation in the incident beam.
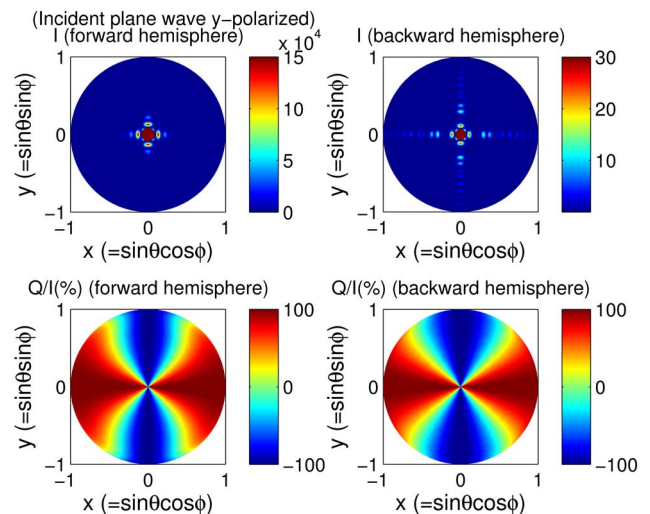


Fig. 6.   Dependence of the Stokes parameters $I$ and $Q$ on scattering angle $\theta$ and azimuth angle $\phi$ (shown as variation with $x = \sin\theta\cos\phi$ and $y = \sin\theta\sin\phi$) for the same cubic array shown in Figs. 3–5 but for Case 2 (see Table 1), i.e., the component spheres are metallic, electrically conducting. The incident plane wave is linearly $y$ polarized.
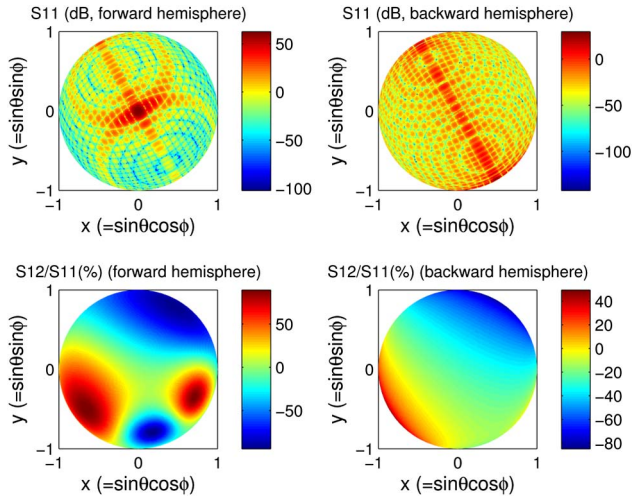
Fig. 7. Dependence of the Mueller matrix element $S_{11}$ and $S_{12}/S_{11}$ on scattering angle $\theta$ and azimuth angle $\phi$ (shown as variation with $x = \sin \theta \cos \phi$ and $y = \sin \theta \sin \phi$) for the same cubic array shown in Figs. 3–6 but for Case 3 (see Table 1), i.e., the Euler-angle triad specifying the orientation of the 3D array is (0°,20°,30°). The Mueller matrix element $S_{11}$ is shown in decibels.

# 5. ADDITIONAL NUMERICAL EXAMPLES: REGULAR PARTICLE ARRAYS WITH A RECTANGULAR OPENING

In practical calculations, the PA-type scattering solutions of GMM are applicable to arrays having a desired overall shape or geometrical structure. For demonstration, two simple examples given in this section are a square and a cubic array with a rectangular opening, illuminated by a $z$-propagating monochromatic plane wave of 31.416 mm wavelength. The latter is just the simple extension of the former in the additional third dimension. The square array consists of $301 \times 301$ identical dielectric spheres of 1 mm diameter and of refractive index (1.6, 0.1), with the inside $201 \times 201$ spheres removed. This 2D structure is in its initial orientation, i.e., all component sphere centers are in the $x$–$y$ plane and the "sides" of the array
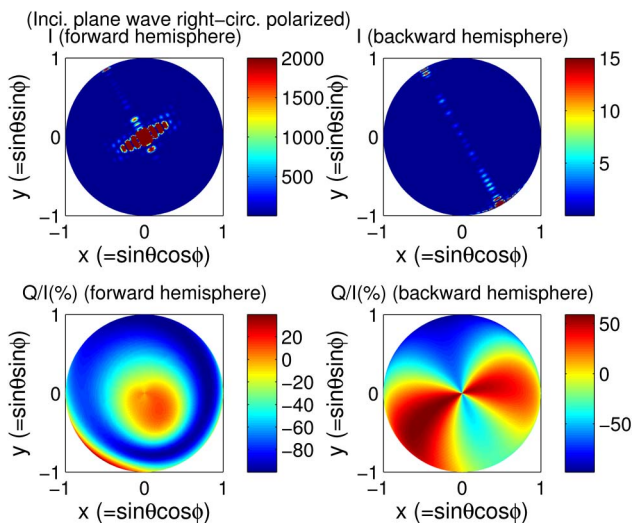


Fig. 8. Dependence of the Stokes parameters $I$ and $Q$ on scattering angle $\theta$ and azimuth angle $\phi$ (shown as variation with $x = \sin \theta \cos \phi$ and $y = \sin \theta \sin \phi$) for the same cubic array in the same Case 3 as shown in Fig. 7. The incident plane wave is right-circularly polarized.

and the window are parallel to the $x$ or $y$ axis, respectively. Along either the $x$ or $y$ directions, adjacent spheres are in contact. Similar to Fig. 4, Fig. 9 displays the spatial distribution of the Stokes parameter $I$ when the incident wave is left-circularly polarized. Shown in the left upper panel is what is usually referred to as the Fraunhofer diffraction pattern of the 2D structure. Similar to Fig. 9, Fig. 10 presents the Stokes parameter $I$ when the incident polarization is right-circular. It refers to the 3D array that is the simple stretch of the 2D array shown in Fig. 9 and thus has a similar inside window opening. In this 3D structure, every component sphere in the 2D structure becomes the same linear chain of 301 contacting spheres. It is clear that the differences between Figs. 9 and 10 are completely due to the extension of the obstacle in the additional dimension, in other words, due to the different geometrical structures and overall shapes of the scattering bodies.

The fascinating physical phenomenon of "diffraction" is of common interest to scientific and technical fields that deal with wave propagation. As far as electromagnetic radiation is concerned, diffraction stems from the complicated interaction of light and other electromagnetic waves with substances present in the path of the electromagnetic radiation. This is exactly what a scattering theory attempts to analyze thoroughly and to interpret precisely. The scattered intensity pattern shown in Fig. 9 for the 2D array with a window closely resembles the observed Fraunhofer diffraction pattern known for a rectangular aperture [27,28]. Powerful diffraction theories, as summarized in excellent books (for example, [27–29]), work satisfactorily in the treatment of many problems concerning diffraction of light. To test the PA version of scattering formulation developed recently, further research efforts would be worthwhile to compare between the scattering and diffraction theories and look deeply into the separate theoretical foundations of the formulations.
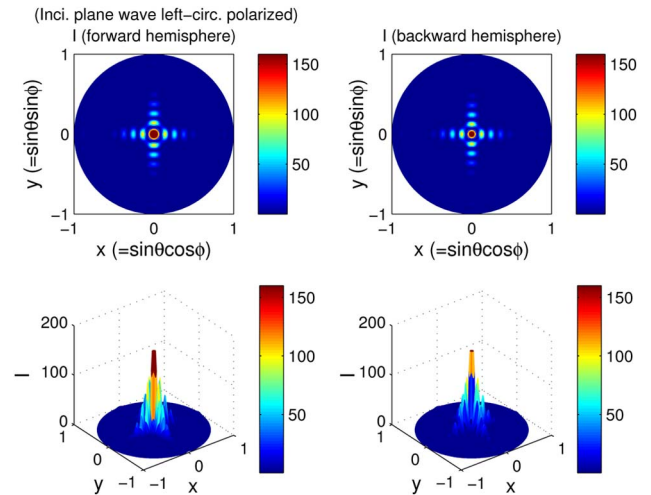


Fig. 9. Dependence of the Stokes parameter $I$ on scattering angle $\theta$ and azimuth angle $\phi$ (shown as variation with $x = \sin \theta \cos \phi$ and $y = \sin \theta \sin \phi$) for a square array consisting of $301 \times 301$ identical dielectric spheres of 1 mm diameter, in which the inside $201 \times 201$ spheres are removed. The refractive index of the spheres is (1.6, 0.1). This 2D structure is illuminated by a monochromatic plane wave of 31.416 mm wavelength. It is in its initial orientation, i.e., all component sphere centers are in the $x$–$y$ plane and the "sides" of the array and the window are parallel to the $x$ or $y$ axis, respectively. Along either the $x$ or $y$ directions, adjacent spheres are in contact. The incident plane wave is left-circularly polarized.
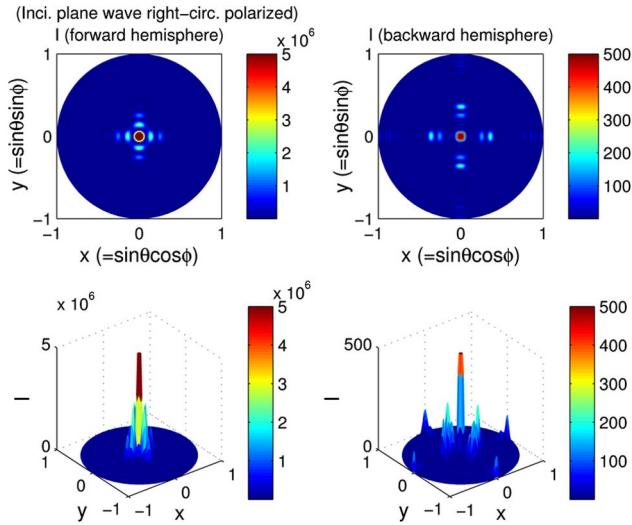
Fig. 10.    Same as Fig. 9 but for a cubic array having a square window opening, which is the simple extension in the $z$ direction of the 2D structure shown in Fig. 9, i.e., every component sphere in the 2D structure becomes the same linear chain of 301 contacting spheres. The incident plane wave is right-circularly polarized.

# 6. DISCUSSION AND FUTURE WORK

The special PA version of scattering formulations of GMM has been extended to the general 3D case, which has potentially useful applications in many related scientific research and engineering areas. One of its obvious advantages is that, when implemented into practical calculations, it can handle a huge number of component particles with no excessive requirements for both computing time and computer memory. This benefit will become more apparent when the physical dimension of the component unit cells gets much smaller than the incident wavelength and the total number of component units gets extremely large.

A theory usually has its particular range of applications and regime of validity. The PA-type scattering formulation of GMM is developed specifically for periodic structures consisting of a large number of identical unit cells. Calculations of scattering from an array with a small or moderate total number of components must still use the standard GMM formulation and follow the GA procedure to assure satisfactory accuracy for numerical solutions. Moreover, the newly developed formulation requires further careful tests in a variety of possible ways, especially systematic experimental verifications and comparisons with other theories.

Classical diffraction theories, particularly those of Huygens, Fresnel, Rayleigh–Sommerfeld, and Kirchhoff, adequately explain various specific cases of the diffraction of light by obstacles and apertures. In some sense, scattering theories such as Mie theory and its extensions can be considered as a kind of rigorous diffraction theory. Since Mie-type scattering formulations and diffraction theories rest on quite separate theoretical bases, it would be beneficial to scrutinize the similarities and differences between the two formulations and to compare their theoretical predictions in various circumstances.

The most time-consuming part in the scattering calculations using the current PA formulation is the evaluation of the total cross section for radiation pressure, which demands a single-centered expansion of the total scattered field and

must translate one by one the partial scattered fields of every component particle into a single, common reference frame. It would be greatly beneficial to have an efficient way to evaluate the $\tilde{C}^l_{mnpm'n'p'}$ and $C^l_{mnpm'n'p'}$ coefficients mentioned in Section 3, which are determined only by the geometrical structure of an array. Such further development would help to considerably improve the efficiency of the scattering solution process. It may also help to broaden the range of applications.

The formulation presented in this work and Paper I can potentially apply to particle arrays having an irregular overall shape. An individual component unit in an array can also have an arbitrarily complex structure, as long as the proper scattering characteristics of an individual particle can be calculated with satisfactory precision. Furthermore, a massive collection of regularly arranged, sufficiently small volumes could be a satisfactory approximation to a myriad of shapes and structures of interest, to which the PA approach could quickly provide approximate scattering solutions. Future research work may include the extension of the current formulations to such useful areas.

## REFERENCES

1. L. V. Lorenz, "Sur la Lumière réfléchie et réfractée par une sphère transparente," in *Oeuvres Scientifiques*, L. de Lorenz and H. Valentiner, revues et annotées (Librairie Lehman et Stage, 1898), pp. 405–529.
2. G. Mie, "Beiträge zur Optik trüber Medien speziell Kolloidaler Metallösungen," Ann. Phys. **25**, 377–445 (1908).
3. Y.-L. Xu, "Electromagnetic scattering by an aggregate of spheres," Appl. Opt. **34**, 4573–4588 (1995).
4. Y.-L. Xu, "Electromagnetic scattering by an aggregate of spheres: far field," Appl. Opt. **36**, 9496–9508 (1997).
5. Y.-L. Xu and R. T. Wang, "Electromagnetic scattering by an aggregate of spheres: theoretical and experimental study of the amplitude scattering matrix," Phys. Rev. E **58**, 3931–3948 (1998).
6. Y.-L. Xu, "Electromagnetic scattering by an aggregate of spheres: asymmetry parameter," Phys. Lett. A **249**, 30–36 (1998).
7. Y.-L. Xu, B. Å. S. Gustafson, F. Giovane, J. Blum, and S. Tehranian, "Calculation of the heat-source function in photophoresis of aggregated spheres," Phys. Rev. E **60**, 2347–2365 (1999).
8. Y.-L. Xu and B. Å. S. Gustafson, "A generalized multiparticle Mie-solution: further experimental verification," J. Quant. Spectrosc. Radiat. Transfer **70**, 395–419 (2001).
9. Y.-L. Xu and N. G. Khlebtsov, "Orientation-averaged radiative properties of an arbitrary configuration of scatterers," J. Quant. Spectrosc. Radiat. Transfer **79–80**, 1121–1137 (2003).
10. Y.-L. Xu, "Radiative scattering properties of an ensemble of variously shaped small particles," Phys. Rev. E **67**, 046620 (2003).
11. Y.-L. Xu, "Scattering Mueller matrix of an ensemble of variously shaped small particles," J. Opt. Soc. Am. A **20**, 2093–2105 (2003).
12. Y.-L. Xu and B. Å. S. Gustafson, "Light scattering by an ensemble of small particles," in *Recent Research Developments in Optics* (Research Signpost, 2003), pp. 599–648.
13. P. C. Waterman, "Matrix formulation of electromagnetic scattering," Proc. IEEE **53**, 805–812 (1965).
14. P. C. Waterman, "New formulation of acoustic scattering," J. Acoust. Soc. Am. **45**, 1417–1429 (1969).
15. P. C. Waterman, "Symmetry, unitarity and geometry in electromagnetic scattering," Phys. Rev. D **3**, 825–839 (1971).
16. P. C. Waterman, "Numerical solution of electromagnetic scattering problems," in *Computer Techniques for Electromagnetics*, R. Mittra, ed. (Pergamon, 1973), pp. 97–157.
17. P. C. Waterman, "Matrix methods in potential theory and electromagnetic scattering," J. Appl. Phys. **50**, 4550–4566 (1979).
18. G. Kristensson and P. C. Waterman, "The *T*-matrix for acoustic and electromagnetic scattering by circular disks," J. Acoust. Soc. Am. **72**, 1612–1625 (1982).

19. P. C. Waterman, "Surface fields and the *T*-matrix," J. Opt. Soc. Am. A **16**, 2968–2977 (1999).
20. P. C. Waterman, "The *T*-matrix revisited," J. Opt. Soc. Am. A **24**, 2257–2267 (2007).
21. GMM public-domain FORTRAN codes are currently available at http://code.google.com/p/scatterlib.
22. Y.-L. Xu, "Scattering of electromagnetic waves by periodic particle arrays," J. Opt. Soc. Am. A **30**, 1053–1068 (2013).
23. A. R. Edmonds, *Angular Momentum in Quantum Mechanics* (Princeton University, 1996).
24. H. C. van de Hulst, *Light Scattering by Small Particles* (Wiley, 1957).
25. C. F. Bohren and D. R. Huffman, *Absorption and Scattering of Light by Small Particles* (Wiley, 1983).
26. M. Kerker, *The Scattering of Light* (Academic, 1969).
27. M. Born and E. Wolf, *Principles of Optics*, 7th ed. (Cambridge University, 1999).
28. J. W. Goodman, *Introduction to Fourier Optics*, 2nd ed. (McGraw-Hill, 1996).
29. J. D. Jackson, *Classical Electrodynamics*, 2nd ed. (Wiley, 1975).